Soft Matter

Deep Indentation and Puncture of a Rigid Cylinder Inserted into a Soft Solid

Journal:	*Soft Matter*
Manuscript ID	SM-ART-10-2020-001775.R3
Article Type:	Paper
Date Submitted by the Author:	23-Apr-2021
Complete List of Authors:	Barney, Christopher; University of Massachusetts Amherst, Polymer Science And Engineering; University of California Santa Barbara, Department of Chemical Engineering; University of California Santa Barbara, Department of Mechanical Engineering Chen, Chao; University of Massachusetts Amherst Department of Polymer Science and Engineering, Crosby, Alfred; University of Massachusetts, Polymer Science and Engineering

Soft Matter

ARTICLE TYPE

Cite this: DOI: 10.1039/xxxxxxxxxx

Deep Indentation and Puncture of a Rigid Cylinder Inserted into a Soft Solid†

Christopher W. Barney,[a] Chao Chen,[a] and Alfred J. Crosby*[a]

Received Date
Accepted Date

DOI: 10.1039/xxxxxxxxxx

www.rsc.org/journalname

Deep indentation and puncture can be used to characterize the large strain elastic and fracture properties of soft solids and biological tissues. While this characterization method is growing in application there are still open questions about deep indentation and puncture, including how the distribution of strains and stresses in the surrounding material relate to the resultant force exerted on the indenter. Direct quantification of the deformation field around a rigid indenter during penetration of a soft solid is necessary to substantiate the current qualitative understanding of these strains and increase the impact and usefulness of puncture tests. Here, the deformation field of a rigid cylinder inserted into a soft solid is quantified using digital image correlation (DIC). DIC measurements are validated by reconstituting the measured nominal force on the cylinder during deep indentation and puncture. The deformation field is used to map the strain field around the indenter during deep indentation and puncture. These measurements provide direct insight into the puncture process and show that while the resultant force mainly arises from the sheared region on the sides of the indenter, the compressed region below the tip is responsible for initiating failure.

1 Introduction

Deep indentation of a rigid body into a soft solid is an important process in bite mechanics and needle insertion.[1–4] Several groups over the last 60 years have highlighted the potential for puncture tests (deep indentation beyond the point of puncture) to be used as a materials characterization method for stiff rubbers;[5–11] however, puncture tests have recently begun to find greater application in characterizing the large strain elastic and fracture properties of soft gels that are difficult to characterize with more traditional methods.[12–15] Deep indentation and puncture differs from small strain contact mechanics as the displacement of the indenter goes to values that are an order of magnitude greater than the radius of the indenter R.[11–15] Deep indentation and puncture of soft solids is also unique as the nominal stresses at the critical point of puncture, or material failure, can be several orders of magnitude greater than the modulus of the material.[12]

While this loading situation is common enough in both nature and laboratory settings, understanding of the deformation field around indenters with blunted tips (i.e. flat and spherical typically used during materials characterization) during puncture has remained elusive.[16] Quantitative understanding of this process has been limited by 1) a breakdown of analytical solutions at deep indentation,[17] 2) large strain gradients observed under small displacements,[5,11] 3) an incomplete understanding of crack path and shape during puncture,[9,11] and 4) complications arising from implementing sharp corners in simulations.[18] Despite the challenges in treating this problem, experiments have produced a qualitative picture of the strain field around an indenter during deep indentation that largely consists of compressive strain below the indenter and shear strain on the sides of the indenter as sketched in Figure 1.[16,19] This qualitative understanding was

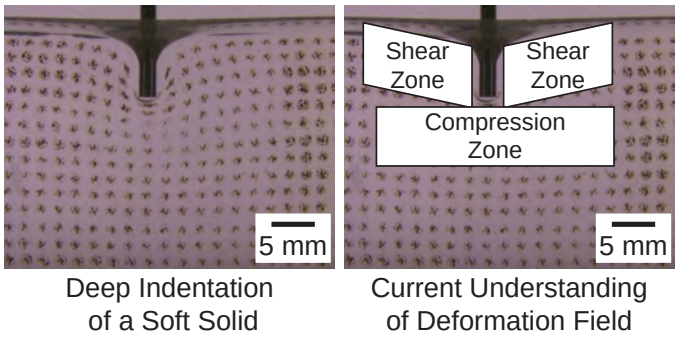

Fig. 1 Images showing deep indentation of a soft solid alongside the current qualitative understanding[16] of the deformation field around the indenter during this process.

[a] Polymer Science and Engineering Department, University of Massachusetts, 120 Governors Drive, Amherst, MA, 01003, USA. Fax: +1 413 545 0082; Tel: +1 423 577 1313; E-mail: acrosby@umass.edu

† Electronic Supplementary Information (ESI) available: [details of any supplementary information available should be included here]. See DOI: 10.1039/cXsm00000x/

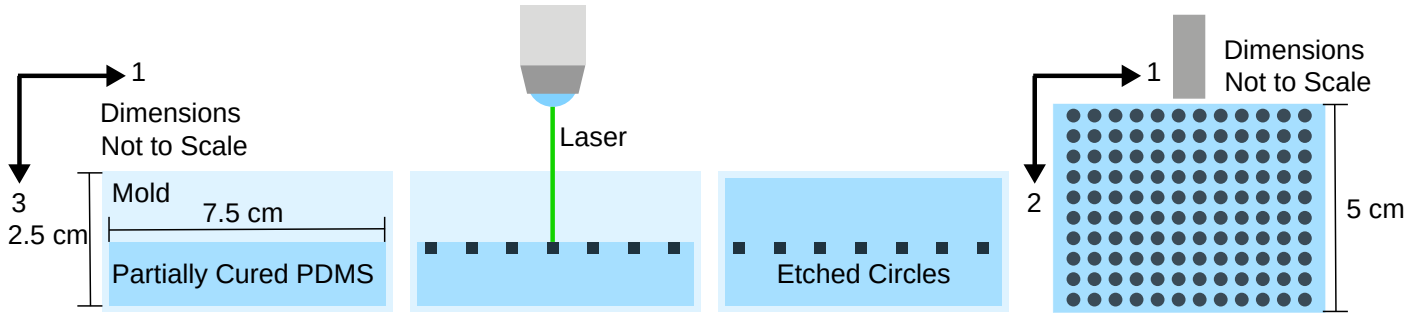

Fig. 2 Sketch showing the preparation steps for PDMS elastomers with an internal plane of optical contrast. 30:1 PDMS that has been mixed and degassed is poured into a mold and partially cured for 30 minutes at 70°C. Then a laser is used to etch a pattern of circles onto the surface and deposit a fine black ash. The remainder of the mold is filled with PDMS and cured for 18 hours at 70°C. Once finished curing, the elastomer is turned on it's side and punctured with a rigid cylindrical indenter.

recently used to solve a residual strain issue in needle-induced cavitation protocols; however, the deformation field around the indenter was only inferred and not directly quantified.[19] Strategies to quantify the deformation around a rigid body inserted into a soft solid are necessary to expand the impact and usefulness of puncture tests as a materials characterization method.

In this work, the deformation field is quantified experimentally using digital image correlation (DIC). Direct quantification of the deformation fields of wedge and conical tipped indenters, commonly used in the medical community, have already been quantified by DIC in the literature.[20,21] DIC is a robust experimental method for quantifying deformation fields through direct visualization of a pattern with optical contrast.[22–24] This technique can be applied in two or three dimensions and has proven particularly useful in characterizing the deformation of soft solids.[25–29] DIC can be very useful when damage occurs during a deformation process. This often leads to a loss of data integrity near the crack itself; however, regions further away from the damage can still be mapped enabling the quantification of the bulk stress state. This work aims to directly quantify the deformation field around a rigid cylinder indented into a soft solid through DIC.

The sections that follow test the current understanding of the deformation field during deep indentation. First the materials and methods used during deep insertion of a rigid cylinder into a soft solid are presented. Then the DIC measurement of the deformation field is validated through a reconstitution of the nominal force on the indenter. Finally, the strain field around the indenter before and after puncture is used to quantitatively confirm the inferred picture of the deformation field. These results have strong implications for characterizing the large strain elastic and fracture properties of soft solids and biological tissues which are often difficult to quantify with traditional methods.

2 Experimental

2.1 Materials

Deep indentation and puncture experiments were conducted on a polydimethylsiloxane (PDMS) elastomer with an internal plane of optical contrast. A Sylgard®184 kit was sourced from Krayden, Inc. and used as received. Samples were mixed and degassed at a prepolymer:crosslinking agent ratio of 30:1. Modeling the small strain regime during indentation with contact mechanics showed that the elastic modulus E of the sample was 556.6 kPa. Preparation of the sample is shown in Figure 2. An acrylic mold with dimensions $7.5 \times 5 \times 2.5$ cm was filled halfway with PDMS. The PDMS was then partially cured for ~30 minutes at 70°C, and the sample was tilted to confirm that the sample was sufficiently cured to resist deformations upon introducing the embedded pattern. To create an internal plane of optical contrast, a pattern of circles was then etched onto the surface using a Universal Laser VLS3.50 laser cutter. The circles had a 1 mm diameter and were spaced in a square array with a 2 mm center-to-center distance. The etching deposited a fine ash pattern of carbon black that provides the optical contrast used for DIC. Once etched, the remainder of the mold was filled with PDMS and cured in the oven at 70°C for 18 hours. The initial partial curing of the PDMS was chosen to anchor the etched pattern while allowing diffusion and bonding across interface during the second curing step, which was long enough to minimize a stiffness gradient between the two halves of the sample. Exploiting this concept of diffusion across an interface and reaction between a formed network and a forming network was inspired by some recent work on topological adhesion that discusses this concept in more detail.[30–32]

2.2 Methods

2.2.1 Puncture.

A rigid steel cylinder with $R = 1$ mm was indented into and retracted from a PDMS elastomer with an internal plane of optical contrast to a maximum displacement of 15 mm at a displacement rate of 1 mm/s. The surface of the indenter was characterized with a Zygo NewView 7300 Optical Surface Profiler. A profile of the probe tip is shown in Figure S4 and gives an estimated root mean square roughness value of 6.35 μm. The indenter was centered over the internal plane of optical contrast. Force and displacement were monitored using a TA.XT Plus Texture Analyzer from Texture Technologies with a 50 N load cell. Visualization of the process was obtained using an EO-1312C color CCD camera from Edmund Optics. Video was captured at a rate of 15.4 frames per second at a resolution of 35 pixels per mm. This leads to a minimum displacement resolution of approximately 30 μm at

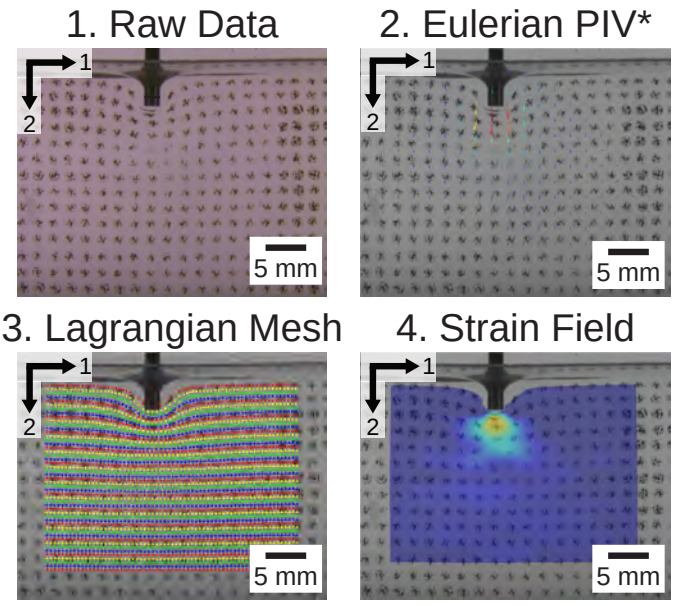

Fig. 3 Images showing the different steps in the DIC process. In order, the raw data is gathered, frame-by-frame displacement fields are measured via an ImageJ plugin developed by Tseng et al.,[33] the Eulerian displacement field is converted to a Lagragian mesh, and this mesh is then used to quantify the strain field around the indenter.

this magnification. A schematic of the setup with plots of the raw data as well as a video of the puncture measurement are shown in Supplementary Figure S1 and Supplementary Video SV1_1. Note that the camera only visualized approximately the top half of the sample height.

2.2.2 Digital Image Correlation (DIC)

A summary of the steps in the DIC process is shown in Figure 3 and each individual step is shown in Supplementary Videos SV1_1-4. First the raw data, which consists of a measurement of the force on the indenter and visualization of the deformation field during the deep indentation and puncture process, is collected. Then an iterative particle image velocimetry (PIV)[34] plugin for ImageJ developed by Tseng et al.[33] is used to measure the frame-by-frame displacement field. This results in an Eulerian grid of local displacement vectors during the puncture process. In order to calculate the local strains, the Eulerian grid is then converted to a Lagrangian mesh. A custom MatLab procedure was developed that introduces a grid of points on the first frame of interest (frame 222), interpolates the displacement field (cubic fitting with the interp2 function which constrains the interpolation so that it matches each input data point) to be a continuous function on each frame, and then uses said function to move each point on the frames until the final frame of the video (frame 757). Full details on the DIC process including the methods used for selecting input parameters are contained in the SI. The Lagrangian Mesh was then used to calculate the deformation gradient F assuming axisymmetry. F was then used to calculate the Green strain ε_{ij} where δ_{ij} is Kronecker's delta.

$$\varepsilon_{ij} = \frac{1}{2}(F_{ki}F_{kj} - \delta_{ij}) \tag{1}$$

3 Reconstituting the Nominal Force

While the DIC process above can quantify the strain field on each frame of the video gathered, it is not immediately clear if the measurement is accurate. In order to verify this, the resultant normal force f along the axial direction of the cylinder was reconstituted from the DIC measurement and compared to the direct measurement from the load cell. Assuming Neo-Hookean behavior gives the true stress,

$$\sigma_{ij} = \frac{E}{3}F_{ki}F_{kj} - p\delta_{ij} \tag{2}$$

where p is the hydrostatic pressure term and is equal to $E/3$ when there is no strain in the system. In order to accurately estimate the stress in the deformed state p must be estimated. Following the force balance approach introduced by Hall et al.,[29] p can be

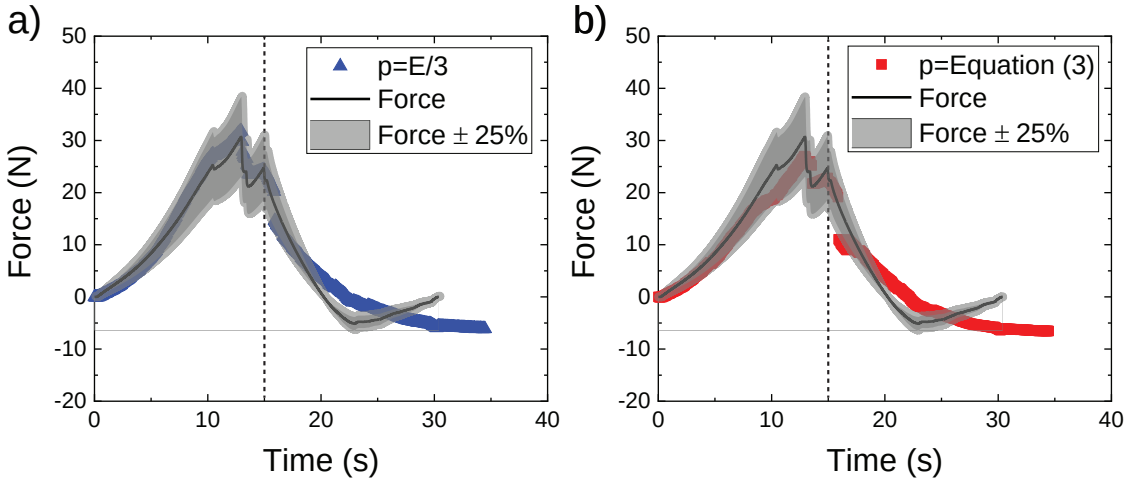

Fig. 4 Comparison between the DIC reconstituted normal force and the load cell data when a) $p = E/3$ and b) when p is modeled by Equation (3). Both force profiles recreated from the DIC stay within 25% up to the point of puncture at 10.3 s. Vertical dashed lines indicate the point at which retraction begins.

estimated at each point in space where $H_{jk}F_{ik} = \delta_{ij}$.

$$p(x_1 + \Delta x) = p(x_1) + \Delta x \sum_{i=1}^{3}\sum_{k=1}^{3}\left(\frac{E}{3}\frac{\partial F_{ik}}{\partial x_k} - p\frac{\partial H_{ik}}{\partial x_k}\right)F_{i1} \quad (3)$$

In order to use Equation (3), the value of p must be known at an initial location. Here it is convenient to treat the leftmost column of unit cells as being far field where no deformations are observed and $p = E/3$.

The force f can then be estimated by summing the total force produced by each unit cell in the top row of unit cells where A_n in the initial area of a unit cell and N_c is the total number of columns. Note that A_n was estimated as a semi-cylinder to avoid double-counting the area. The angle between the 1 direction in the reference and deformed states is represented as θ.

$$f_{22} = \sum_{n=1}^{N_c}\frac{A_n(\sigma_{22}\cos(\theta) + \sigma_{12}\sin(\theta))}{\sqrt{2\varepsilon_{22}+1}} \quad (4)$$

Plots comparing the DIC force profiles when using $p = E/3$ and when using Equation (3) to values measured by the load cell are shown in Figure 4. The vertical dashed line indicates the point at which retraction begins. The full displacement-time profile is shown in Supplementary Figure S1. Assuming $p = E/3$ throughout the sample leads to a larger estimation in the force and a curvature during loading that is greater than that measured by the load cell. Reconstituting the force with Equation (3) gives a lower value of the force, which more closely matches the curvature observed in the measured load cell data. Both force profiles

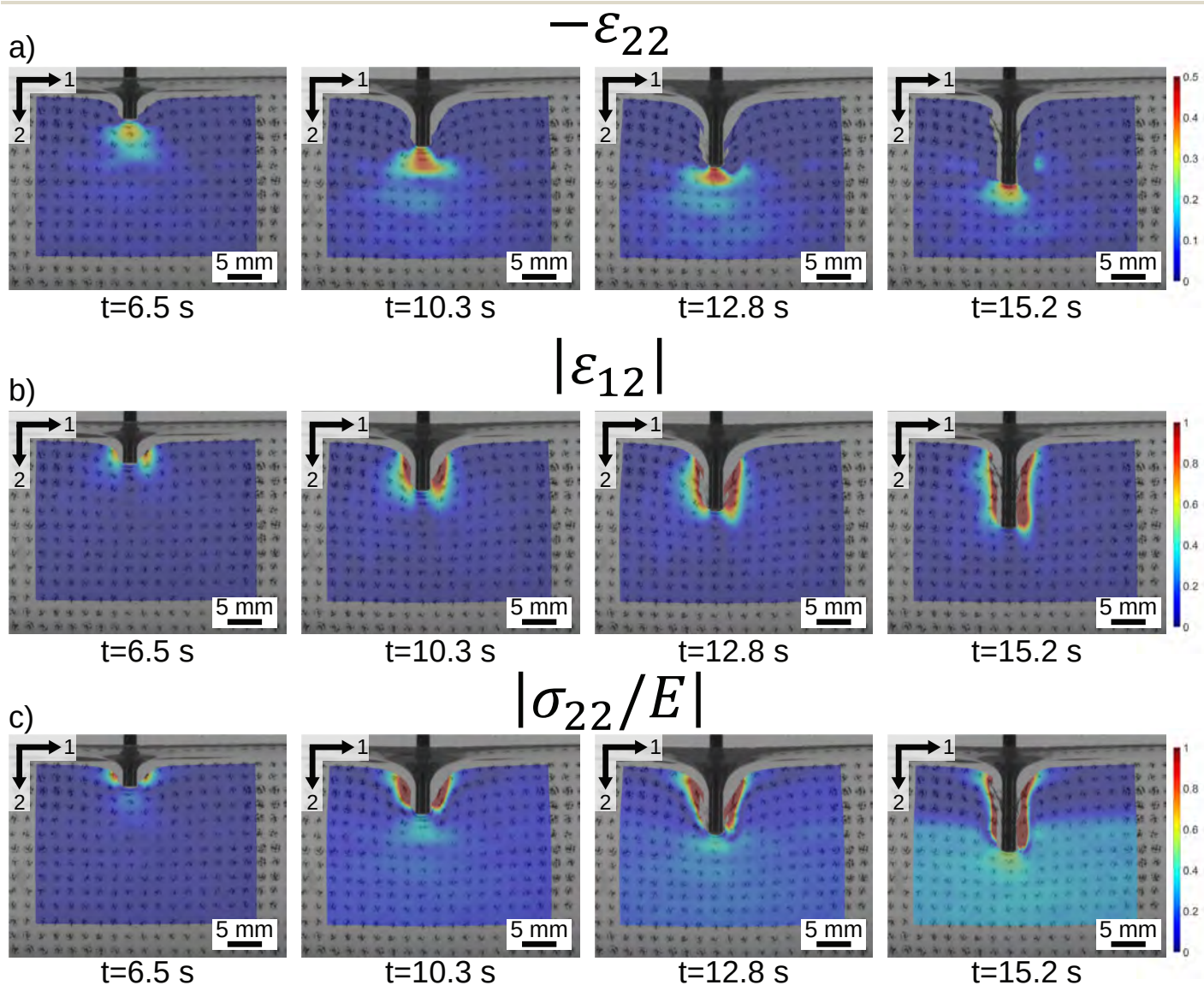

Fig. 5 a) Image of the compressive strain field around the indenter at different time points up to the point of retraction. b) Image of the shear strain field around the indenter at different time points up to the point of retraction. These maps show that the strain field is mainly composed of compression below the indenter and shear on the sides. c) Image of the stress field around the indenter at different time points up to the point of retraction. This distribution shows that the resistance to puncture is greater on the sides of the indenter than it is below.

recreated from the DIC stay within 25 % of the measured force up to the point of puncture. Also, deviation from the trend measured by the load cell is not observed until significant retraction of the indenter occurs. This agreement indicates that the DIC is capable of quantifying the strain field up to the point of retraction at $t = 15.2$ s. The deviation of the force from that measured by the load cell is likely due to a combination of an accumulation of displacement errors during the DIC process and the removal of points during the fracture process.

While the two-step curing process is necessary to establish a plane of optical contrast, we recognize that this procedure could alter the axial symmetry of the elastomer and hence influence the accuracy of certain assumptions in our DIC analysis. We do not observe any evidence for this influence, and furthermore, our results indicate that the two-step cure process has negligible influence. The elastic modulus of the two-step cured material, as measured during deep indentation of the probe, is consistent with one-step cure materials, and our predicted force-displacement relationship from the DIC analysis, which assumes axisymmetry, matches well.

It is somewhat remarkable that the material behavior is well-modeled with a Neo-Hookean constitutive response as polymer networks can often stiffen under large strains. The agreement of the Neo-Hookean DIC estimate with the force data suggests that these mechanisms of stiffening are not observed during deep indentation and puncture of this particular silicone. It is also possible that any stiffening effects are concentrated in the small volume of material experiencing large deformations.

4 Strain Distribution Around Indenter

The distribution of strain around the indenter at different times up to the point of retraction is shown in Figure 5. The compressive strain field is shown in Figure 5a (supplementary video SV1_4) and indicates that compression is mainly observed below the tip of the indenter and not on the sides. The shear strain field is shown in Figure 5b (supplementary video SV1_5) and indicates that shear is mainly observed on the sides of the indenter and not below the tip. Together, these results quantitatively support the previously inferred picture of the strain field around a rigid body indenting into a soft solid.[16,19] This finding is significant as quantitative knowledge of the strain distribution during puncture has remained elusive. This quantitative measurement provides new insight into materials properties and geometries that can be used to prevent or enhance puncture processes.

DIC measurements can also be used to quantify the stress field around the indenter. Figure 5c (supplementary video SV1_6) shows a map of $|\sigma_{22}/E|$ up to the point of retraction. These results indicate that the stress is greater on the sides of the indenter than it is below. Note here that the highest values of σ_{22} are concentrated in the shear zones on the sides of the indenter. That a shear strain can produce a normal stress is evident from Equation (2), where the stress depends on the right Cauchy-Green deformation tensor $F_{ki}F_{kj}$ showing that deformation in a given direction may result in stress in another direction. For example, σ_{22} will be influenced by the deformation gradient in the 2 direction on the 2 face F_{22}, but will also have contributions from F_{12} and F_{32}. This suggests that the bulk resistance of the material to puncture mainly arises from the deformed material on the sides of the indenter and not the material below the indenter.

While the stresses are greater on the sides of the indenter, the crack appears to initiate in the region below the tip. This can be seen in Figure 6 which shows an overlay of the frame-to-frame difference in the compressive strain and stress fields (Supplementary Videos SV1_11 and SV1_12 respectively) on the frames immediately before, during, and after the critical puncture event. The release of stress and strain in the compressive zone indicates that this is where the failure initiates. This suggests that the stress concentration around the tip also plays an important role in the deep indentation and puncture process because it initiates the failure process. The observation that the crack nucleates in the region of lower stress below the indenter tip is somewhat surprising. Previous work in this area has identified that indenter shape[9,10] as well as materials properties and defects[11] influence the crack morphology observed during puncture tests. As apparent in Figure 6, the crack appears to nucleate at an optical marker below the indenter which acts as a critical material defect.

Together, these observations highlight the interplay between the compressed and sheared regions around the indenter. The resultant force mainly arises from the sheared region on the sides of the indenter in which greater deformation is only possible so long as failure does not initiate in the compressed region below the tip. This suggests that the ultimate force needed to puncture a material can be reduced when stress is concentrated below the indenter tip to initiate failure in the compressive region at lower penetration depths.

While our DIC process has provided important insight into deep indentation and the intial stages of puncture, it is important to also discuss the limitations of our findings. In particular, the exact strain distribution will depend upon the probe geometry and the constitutive relationship of the indented material. In the study reported here, we have considered a single probe geometry and a single indented material system. Based on previously reported study from our research group as well as others,[5,10–15] quantitative similarity in the deep indentation force-displacement curve up to and just after puncture initiation provides strong indication that the strain distribution through these stages will be similar across a wide range of materials and conditions. However, after puncture is initiated, the shape of the fracture path can give rise a diversity of force-displacement relationships and final fracture patterns.[11] This observation suggests that the particular strain distribution as fracture proceeds post-puncture may be different for different materials and conditions. While our verification steps suggest that our reported DIC results provide an accurate description of strain in our system, the presence of defects, such as the etched optical markers, may influence the exact strain distribution compared to a material system with a different structural morphology. Nonetheless, the results prior to and at the puncture initiation process reported here provide new, broadly applicable insight into the important mechanics of deep indentation and puncture. The results post-puncture also provide interesting observations for how fracture paths and associated strain distributions develop.

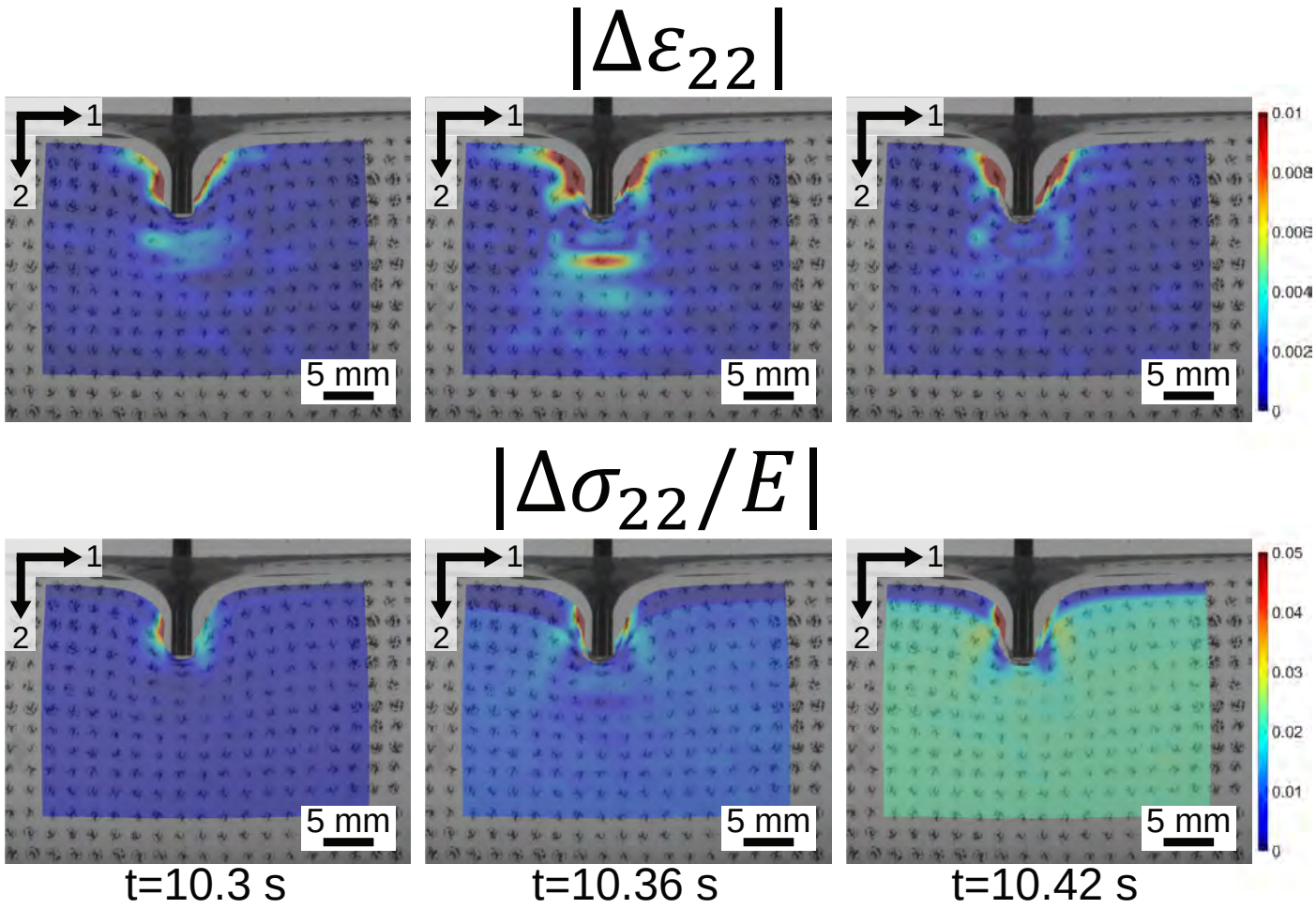

Fig. 6 Images of the frame-to-frame difference of the compressive strain ($|\Delta\varepsilon_{22}|$) and stress ($|\Delta\sigma_{22}/E|$) field on the frames immediately before, during, and after the critical event. The release of compressive strain shows that the crack initiates in the compressive zone below the indenter tip.

5 Conclusions

DIC was combined with deep insertion of a rigid cylinder into a soft elastomer with an internal plane of optical contrast. DIC measurements were demonstrated to be accurate by reconstituting the nominal force on the cylinder during the puncture process. Mapping of the strain field was then used to validate that the strain around the indenter consists mainly of compression below the indenter tip and shear on the sides. Mapping of the stress field was used in order to reveal the interplay between the compressed and sheared regions during deep indentation and puncture. Understanding this deformation field will increase the impact of puncture tests as a method for characterizing the large strain elastic and fracture properties of soft materials.

6 Acknowledgements

The authors acknowledge the support of the Office of Naval Research (ONR grant number N00014-17-1-2056). The authors would also like to thank Hongbo Fu for gathering the optical profilometry data on the indenter tip.

7 Conflicts of Interest

The authors have no conflicts of interest to declare.

References

1 M. K. Ramasubramanian, O. M. Barham and V. Swaminathan, *Bioinspiration and Biomimetics*, 2008, **3**, 1–10.
2 S. E. Santana, E. R. Dumont and J. L. Davis, *Functional Ecology*, 2010, **24**, 776–784.
3 A. M. Okamura, C. Simone and M. D. O'Leary, *IEEE Transactions on Biomedical Engineering*, 2004, **51**, 1707–1716.
4 W. K. Cho, J. A. Ankrum, D. Guo, S. A. Chester, S. Y. Yang, A. Kashyap, G. A. Campbell, R. J. Wood, R. K. Rijal, R. Karnik, R. Langer and J. M. Karp, *Proceedings of the National Academy of Sciences*, 2012, **109**, 21289–21294.
5 D. I. Livingston, G. S. Yeh, P. Rohall and S. D. Gehman, *Journal of Applied Polymer Science*, 1961, **V**, 442–451.
6 G. S. Yeh and D. I. Livingston, *Rubber Chemistry and Technology*, 1961, **34**, 937–952.
7 D. I. Livingston and L. E. Hildenbrand, *Rubber Chemistry and Technology*, 1964, **37**, 14–27.
8 K. Ab-Malek and A. Stevenson, *Journal of Materials Science*, 1984, **19**, 585–594.

9 A. Stevenson and K. Ab Malek, *Rubber Chemistry and Technology*, 1994, **67**, 743–760.

10 O. a. Shergold and N. a. Fleck, *Proceedings of the Royal Society A: Mathematical, Physical and Engineering Sciences*, 2004, **460**, 3037–3058.

11 W.-c. Lin, K. J. Otim, J. L. Lenhart, P. J. Cole and K. R. Shull, *Journal of Materials Research*, 2009, **24**, 957–965.

12 S. Fakhouri, S. B. Hutchens and A. J. Crosby, *Soft matter*, 2015, **11**, 4723–4730.

13 S. Rattan and A. J. Crosby, *Extreme Mechanics Letters*, 2018, **24**, 14–20.

14 S. Rattan, L. Li, H. K. Lau, A. J. Crosby and K. L. Kiick, *Soft Matter*, 2018, **14**, 3478–3489.

15 S. Rattan and A. J. Crosby, *ACS Macro Letters*, 2019, **8**, 492–498.

16 S. Fakhouri, *PhD thesis*, 2015.

17 I. N. Sneddon, *International Journal of Engineering Science*, 1965, **3**, 47–57.

18 M. L. Dunn, W. Suwito, S. Cunningham and C. W. May, *International Journal of Fracture*, 1997, **84**, 367–381.

19 C. W. Barney, Y. Zheng, S. Wu, S. Cai and A. J. Crosby, *Soft Matter*, 2019, **15**, 7390–7397.

20 W. Zhang, Y. Ma and Z. Li, *Medical Physics*, 2016, **43**, 505–512.

21 A. Leibinger, A. E. Forte, Z. Tan, M. J. Oldfield, F. Beyrau, D. Dini and F. Rodriguez y Baena, *Annals of Biomedical Engineering*, 2016, **44**, 2442–2452.

22 J. Toyjanova, E. Bar-Kochba, C. López-Fagundo, J. Reichner, D. Hoffman-Kim and C. Franck, *PLoS ONE*, 2014, **9**, 1–12.

23 E. Bar-Kochba, J. Toyjanova, E. Andrews, K. S. Kim and C. Franck, *Experimental Mechanics*, 2015, **55**, 261–274.

24 A. K. Landauer, M. Patel, D. L. Hennan and C. Franck, *Experimental Mechanics*, 2018, **58**, 815–830.

25 A. Chateauminois and C. Fretigny, *Eur. Phys. J. E*, 2008.

26 T. Nguyen Danh, P. Paolino, M. Audry, A. Chateauminois, C. Frétigny, Y. Le Chenadec, M. Portigliatti and E. Barthel, *The Journal of Adhesion*, 2011, **87**, 235–250.

27 A. Chateauminois, D.-T. Nguyen and C. Frétigny, *Sot Matter*, 2017.

28 S. Mzabi, D. Berghezan, S. Roux, F. Hild and C. Creton, *Journal of Polymer Science, Part B: Polymer Physics*, 2011, **49**, 1518–1524.

29 M. S. Hall, R. Long, C.-y. Hui and M. Wu, *Biophysical Journal*, 2012, **102**, 2241–2250.

30 S. Cheng, C. Yang, X. Yang and Z. Suo, *Extreme Mechanics Letters*, 2020, **38**, 100756.

31 J. Steck, J. Kim, J. Yang, S. Hassan and Z. Suo, *Extreme Mechanics Letters*, 2020, **39**, 100803.

32 J. Yang, J. Steck, R. Bai and Z. Suo, *Extreme Mechanics Letters*, 2020, **40**, 100891.

33 Q. Tseng, E. Duchemin-Pelletier, A. Deshiere, M. Balland, H. Guillou, O. Filhol and M. Thery, *Proceedings of the National Academy of Sciences*, 2012, **109**, 1506–1511.

34 R. J. Adrian, *Experiments in Fluids*, 2005, **39**, 159–169.